



**HAL**  
open science

# Large Field-Like spin-orbit torque and magnetization manipulation in a full epitaxial van der Waals 2D-ferromagnet/Topological-insulator heterostructure grown by molecular beam epitaxy

N. Figueiredo-Prestes, S. Krishnia, J. Peiro, V. Zatzko, B. Dlubak, N. Reyren, H. Jaffrès, P. Seneor, J.-M. George, P. Tsipas, et al.

## ► To cite this version:

N. Figueiredo-Prestes, S. Krishnia, J. Peiro, V. Zatzko, B. Dlubak, et al.. Large Field-Like spin-orbit torque and magnetization manipulation in a full epitaxial van der Waals 2D-ferromagnet/Topological-insulator heterostructure grown by molecular beam epitaxy. *Physical Review Applied*, 2023, 19 (1), pp.014012. 10.1103/PhysRevApplied.19.014012 . hal-04226759

**HAL Id: hal-04226759**

**<https://hal.science/hal-04226759>**

Submitted on 3 Oct 2023

**HAL** is a multi-disciplinary open access archive for the deposit and dissemination of scientific research documents, whether they are published or not. The documents may come from teaching and research institutions in France or abroad, or from public or private research centers.

L'archive ouverte pluridisciplinaire **HAL**, est destinée au dépôt et à la diffusion de documents scientifiques de niveau recherche, publiés ou non, émanant des établissements d'enseignement et de recherche français ou étrangers, des laboratoires publics ou privés.

Large Field-Like spin-orbit torque and magnetization manipulation in a full epitaxial  
van der Waals 2D-ferromagnet/Topological-insulator heterostructure grown by  
molecular beam epitaxy

N. Figueiredo-Prestes<sup>1</sup>, S. Krishnia, J. Peiro, V. Zatkan, B. Dlubak, N. Reyren, H. Jaffrès, P. Seneor, J.-M. George<sup>2</sup>

Unité Mixte de Physique, CNRS, Thales, Université Paris-Saclay, 91767, Palaiseau, France.

P. Tsipas, P. Pappas, S. Fragkos\*, A. Lintzeris\*\*, S. Chaitoglou, A. Dimoulas  
National Center for Scientific Research DEMOKRITOS, Institute of Nanoscience and Nanotechnology, 15341, Athens, Greece.

\* Also at: Department of Mechanical Engineering, University of West Attica, 12241 Athens, Greece

\*\* Also at: Department of Physics, National Technical University of Athens, 15780 Athens, Greece

M. Heuken

AIXTRON SE, Herzogenrath, Germany

## Abstract

With the development of novel technologies taking advantage of emerging quantum phenomena at extreme conditions of dimensionality and temperature, the search for new materials and heterostructures engineering has opened up in several fronts. Here we report the magnetotransport properties of topological insulator/2D-ferromagnet (TI/2D-FM) heterostructures composed of  $\text{Cr}_{1+\delta}\text{Te}_2/\text{Bi}_2\text{Te}_3$  stacks grown by molecular beam epitaxy (MBE). The electrical transport measurements revealed high levels of Field-Like effective torques, up to 115 mT at a current density of  $10^7$  A/cm<sup>2</sup>, the occurrence of interfacial magnetoresistance effects, such as the Anisotropic Interfacial Magnetoresistance (AIMR), and anomalies in the Anomalous Hall effect. Furthermore, we report on complementary characterization with scanning tunneling microscopy, angle-resolved photoemission spectroscopy, and SQUID measurements. Finally, magnetization reversal induced by current pulses is also reported. The reported results make evident the relevance of the TI/2D-FM interface and indicate the preservation of polarized surface states at the interface.

## 1. INTRODUCTION

---

Authors to whom correspondence should be addressed: <sup>1</sup>[nicholas.figueiredo@cns-thales.fr](mailto:nicholas.figueiredo@cns-thales.fr),  
<sup>2</sup>[jeanmarie.george@cns-thales.fr](mailto:jeanmarie.george@cns-thales.fr)

Efficient manipulation of magnetization states is a key goal in modern spintronics and materials science research in general [1]. To this end, various mechanisms have been explored, from the use of actual magnetic fields to the use of spin-polarized currents in spin-transfer torque (STT) phenomena. More recently, an emerging technology based on the use of pure spin currents has been intensively studied. This mechanism, called spin-orbit torque (SOT), takes advantage of spin accumulation and spin-dependent scattering effects arising in materials and interfaces with high spin-orbit coupling to generate pure spin currents and torques [2]. One class of such materials is the topological insulators (TI), which have attracted interest in recent years based on predictions [3,4], and experimental observations [5,6] of their functionality as a source of high values of SOT. Spin-Hall angle values for TIs have been reported to be at least an order of magnitude larger than those found for metallic alloys, which could lead to reduced critical currents for magnetization switching, a key requirement for the widespread adoption of spintronic memory cells [7,8]. The integration of metallic magnetic materials into TIs brings its own challenges, particularly with respect to the stability of the topological surface states at the TI/ferromagnet interface [9,10]. In addition, the metallic films are much less resistive than the TI layer, resulting in less efficient spin current generation since much of the applied current flows in the more conductive magnetic layer than in the TI. In the last decade, however, room-temperature ferromagnetic ordering in metallic 2D van der Waals materials has been demonstrated on a scale of a few atomic layers or less [11–14]. In particular, the integration of 2D ferromagnets (2D-FM) on chemically and structurally compatible TI may benefit from the sharply defined van der Waals FM/TI interfaces, which ensures optimal coupling for the generation of SOT. In addition, the higher resistivity of these 2D-FM layers could enable electrical probing of the magnetization state with limited current shunting and exploitation of the full SOT efficiency. Moreover, several 2D-FM layers may host skyrmions that are directly evidenced in magnetic imaging experiments [15,16] or reveal their presence indirectly via the topological Hall effect (THE) [17,18], opening the way for novel skyrmion-based spintronic applications.

In this work, we report the integration of TI's and 2D-FM materials in the form of  $\text{Cr}_{1+\delta}\text{Te}_2/\text{Bi}_2\text{Te}_3$  heterostructures.  $\text{Bi}_2\text{Te}_3$  is a layered TI material and  $\text{Cr}_{1+\delta}\text{Te}_2$  is a 2D FM material with low Curie temperature, where each chemically ordered Te/Cr/Te

trilayer ( $\text{CrTe}_2$  TL) is weakly coupled to the next TL through additional interlayer Cr atoms. The  $\delta$  represents, in this case, the extra self-intercalated Cr atoms. Magnetic and electrical properties of MBE grown sapphire (substrate)/ $\text{WS}_2$  (1 ML)/ $\text{Cr}_{1+\delta}\text{Te}_2$  (7 or 10 TL)/ $\text{Bi}_2\text{Te}_3$  (10 QL) layers were characterized using SQUID magnetometry and low-temperature transport measurements (ML stands for monolayer, QL for quintuple layers). Other samples covered with 1 nm Al or 19 nm W were also studied and used for comparison. A list of the samples used in this study can be found in the supplementary (Table T1) [19]. Second-harmonic techniques were used to investigate the spin-to-charge conversion and subsequent SOT at the TI/2D-FM interfaces. This system proved to be a suitable framework to probe the spin-current generation efficiency at the topological insulator interface due to the high resistivity of the  $\text{Cr}_{1+\delta}\text{Te}_2$  films. The torque measurements showed the occurrence of current-induced magnetic torques with a large contribution from the field-like (FL) torque component, which has not been reported before. It was found that the FL effective field in  $\text{Cr}_{1+\delta}\text{Te}_2/\text{Bi}_2\text{Te}_3$  is  $\approx 10$  times larger than the damping-like (DL) component. Such a large value is compatible with the expected results of charge-to-spin conversion induced by the Rashba-Edelstein effect at the TI/2D-FM interface [20–22]. Additional evidence for the presence of polarized interface states comes from the observation of a positive angular dependence for the longitudinal resistance with in-plane saturating fields. This positive magnetoresistance component is inconsistent with the usual spin-Hall magnetoresistance (SMR) and has been associated with an interfacial contribution to the spin-to-charge interconversion [23]. Furthermore, magnetization switching experiments induced by pulsed current were performed in the  $\text{Bi}_2\text{Te}_3/\text{Cr}_{1+\delta}\text{Te}_2$  bilayer, showing partial but consistent reversal with field and current symmetries as expected from SOT. We also observe a large THE-like signal in  $\text{Cr}_{1+\delta}\text{Te}_2/\text{Bi}_2\text{Te}_3$  bilayers up to 110K.

## 2. RESULTS AND DISCUSSION

### A. MBE Growth

Chromium telluride 2D van der Waals ferromagnetic thin films are grown by molecular beam epitaxy on different substrates in the temperature range between 220 and 490 °C with a Cr deposition rate of 0.06 Å/s. The chromium telluride films are covered with topological insulator  $\text{Bi}_2\text{Te}_3$  which serves as SOT material for spin

torque measurements, while others are covered with W and Al ( $\text{AlO}_x$ ) for comparison. The phase diagram of chromium telluride is complex, ranging from  $\text{CrTe}_2$  to Cr-rich  $\text{Cr}_5\text{Te}_8$ ,  $\text{Cr}_2\text{Te}_3$  and  $\text{Cr}_3\text{Te}_4$  phases [24], obtained by spontaneous Cr self-intercalation in the interlayer van der Waals gaps. The Cr rich compounds tend to form at higher temperatures and larger thicknesses and typically result in multiphase material. At low temperature growth (220 °C), chromium telluride films adopt a  $1\times 1$   $\text{CrTe}_2$  surface phase as opposed to higher temperature growth where extra phases (see supplementary [19]), coexisting with the previous one, appear. These high temperature phases are identified from the  $2\times 1$  and  $2\times 2$  superstructures attributed to  $\text{Cr}_3\text{Te}_4$  and  $\text{Cr}_5\text{Te}_8$ , respectively [24]. In this work, we focused our attention to the low temperature grown chromium telluride magnetic films which are single phase materials with well-defined magnetic properties exhibiting strong perpendicular magnetic anisotropy (PMA), about  $0.04 \text{ MJ/m}^3$  at 100 K, large saturation magnetization (0.2 MA/m at 10 K) and high coercivity, up to 1 T at 10 K (see supplementary [19]).

Reflection high-energy electron diffraction (RHEED) and high-resolution scanning tunneling microscopy (STM), shown in Figs. 1(a) and (b), reveal relatively sharp  $1\times 1$  reconstructions patterns pointing to the occurrence of  $\text{CrTe}_2$  phase [24]. The angle resolved photoelectron spectroscopy (ARPES) measurements and Raman spectra (the two characteristic peaks ( $98$  and  $135 \text{ cm}^{-1}$ )) are also comparable to reported results for the  $1\text{T-CrTe}_2$  phase [13,25,26]. However, the particular magnetic properties observed in these samples, namely the low temperature ferromagnetic transition and the out-of-plane anisotropy, have been mostly associated to the  $\text{Cr}_2\text{Te}_3$  phase ( $\delta = 1/3$ ) [27,28] even though the strained  $\text{CrTe}_2$  could also exhibit PMA phases [25,29]. This conflict reflects the inherent difficulty in distinguishing the two phases since the additional interlayer Cr atoms preserve the periodicity along the normal of the  $\text{CrTe}_2$  TLs. Additionally, the lower density of Cr atoms in the interlayers result in black contrast in high-resolution transmission electron microscopy images which can be mistakenly interpreted as Van der Waals gaps [30,31]. In the next few paragraphs we will discuss the magnetotransport results for the low temperature grown Cr-Te based 2D-FM irrespectively of the specific concentration of self-intercalated Cr atoms, if any.

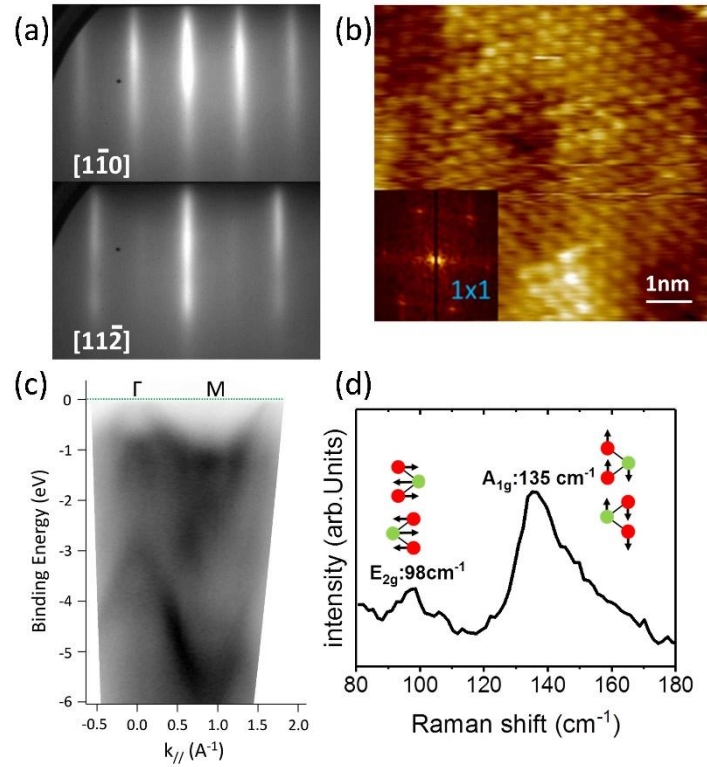


Figure 1: (a) RHEED patterns of the low temperature growth  $\text{Cr}_{1+\delta}\text{Te}_2$  phase (b) High resolution STM real space image along with the FFT showing a  $1\times 1$  pattern of the hexagonal  $\text{Cr}_{1+\delta}\text{Te}_2$ . (c) In-situ ARPES image using a He I excitation energy 21.22 eV along the  $\Gamma$ M direction of the Brillouin zone (d) Raman spectra for the low temperature grown  $\text{Cr}_{1+\delta}\text{Te}_2$  film with the characteristic peaks at  $E_{2g}$ : 98 and  $A_{1g}$ : 135  $\text{cm}^{-1}$ .

## B. Topological Hall Effect

At low temperatures, Hall measurement performed on either the Al-capped  $\text{Cr}_{1+\delta}\text{Te}_2$  films or on the  $\text{Cr}_{1+\delta}\text{Te}_2$  (7 or 10 TL)/ $\text{Bi}_2\text{Te}_3$  bilayer heterostructures grown on sapphire/ $\text{WS}_2$  (1 ML) are characterized by an anomalous Hall effect (AHE) signal typically observed in materials with PMA, *i. e.*, square hysteretic resistance curves with clear saturation values, as it can be seen in Fig. 2(a). The AHE amplitudes, however, depend strongly on the temperature and even changes its sign at several temperatures. At inversion points, the Hall data display anomalies that are characterized by peaks of transversal resistance with amplitudes surpassing the saturation value, Fig. 2(b). Such anomalies have been explained by the emergent magnetic field due to the phase gained by the electrons flowing through skyrmions, giving rise to the topological Hall effect (THE) [32–34]. In our system the symmetry breakage at the interface may enhance the DMI, making possible the stabilization of skyrmions. Sharp potential gradients at the interface may also provide additional contributions to the AHE, resulting in features similar to the THE [35,36].

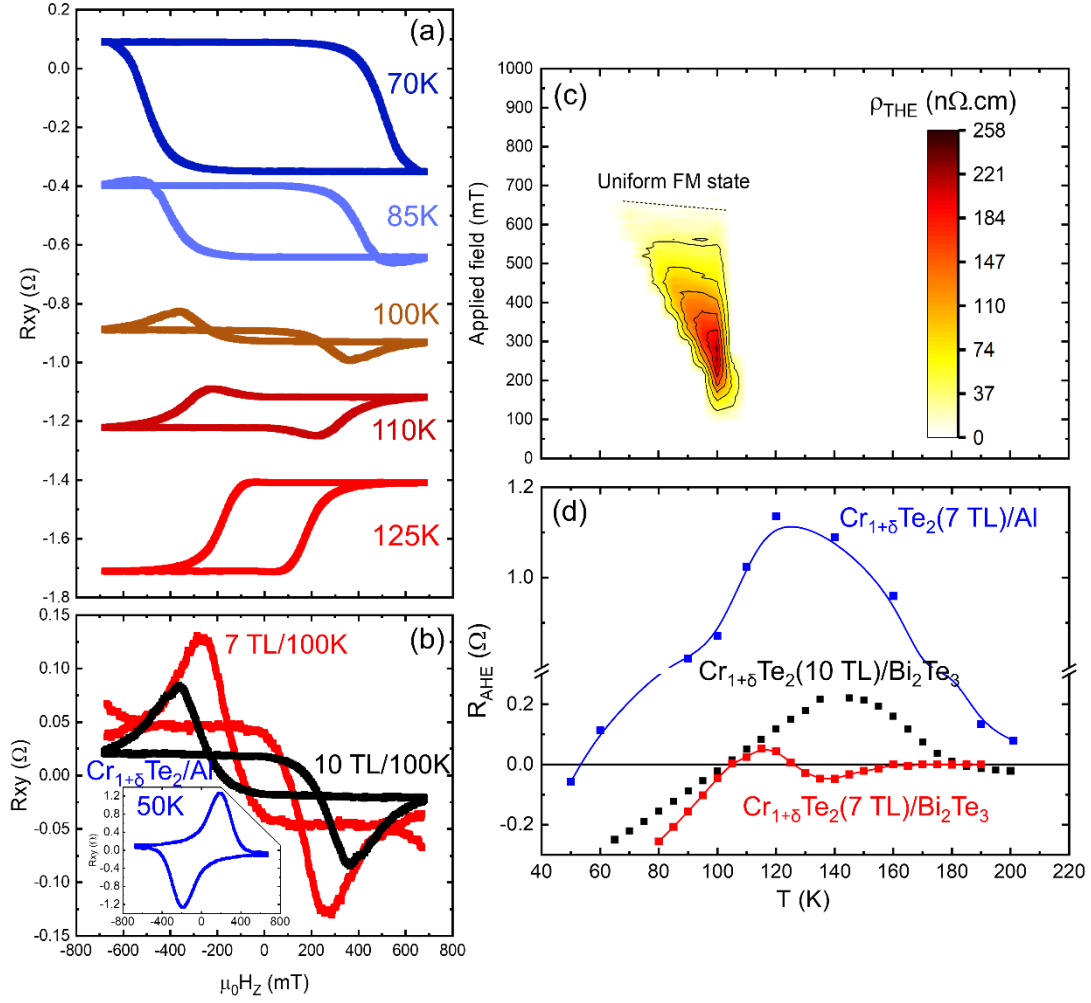


Figure 2: (a) AHE curves at low temperatures for  $\text{Cr}_{1+\delta}\text{Te}_2$  (10 TL)/ $\text{Bi}_2\text{Te}_3$ . (b) AHE curves for  $\text{Cr}_{1+\delta}\text{Te}_2$  (7 or 10 TL)/ $\text{Bi}_2\text{Te}_3$  and  $\text{Cr}_{1+\delta}\text{Te}_2$  (7 TL)/Al samples close to the respective AHE inversion points. The THE signal in Al and  $\text{Bi}_2\text{Te}_3$ -capped samples are reversed due to the opposite signs of the ordinary Hall effect in these structures. (c) THE amplitude as a function of the applied positive field and temperature after negative saturation for a sample of  $\text{Cr}_{1+\delta}\text{Te}_2$  (7 TL)/ $\text{Bi}_2\text{Te}_3$ . (d) Amplitude of the AHE for the different samples as a function of the temperature.

For Al-capped  $\text{Cr}_{1+\delta}\text{Te}_2$ , THE-like features are observed around 50K reaching peak values of about  $1 \mu\Omega\cdot\text{cm}$ . This is comparable with recent observations of giant THE in  $\text{Bi}_2\text{Te}_3/\text{Cr}_{1+\delta}\text{Te}_2$  bilayers where THE values were reported to reach up to  $1.5 \mu\Omega\cdot\text{cm}$  at 10K [17]. Here, however, the peak of the THE for  $\text{Bi}_2\text{Te}_3$ -capped CrTe films occurs at higher temperatures, at about 100 K. The maximum THE values were found to be  $259 \text{ n}\Omega\cdot\text{cm}$  and  $193 \text{ n}\Omega\cdot\text{cm}$  for samples consisting of 7 and 10 trilayers, respectively. The skyrmion sizes were estimated to be about 42 nm, 175 nm and 190 nm for  $\text{Cr}_{1+\delta}\text{Te}_2$  (7 TL)/Al,  $\text{Cr}_{1+\delta}\text{Te}_2$  (7 and 10 TL)/ $\text{Bi}_2\text{Te}_3$ , respectively, which compares well with previously reported value of 34 nm in the  $\text{Cr}_{1+\delta}\text{Te}_2/\text{Bi}_2\text{Te}_3$  heterostructure [18] and with our numerical estimations in single layer  $\text{Cr}_{1+\delta}\text{Te}_2$ . Details on the atomistic simulations and the size estimation can be found in the supplementary [19]. The

inversion of THE polarity observed in  $\text{Cr}_{1+\delta}\text{Te}_2/\text{Al}$  when compared to  $\text{Cr}_{1+\delta}\text{Te}_2/\text{Bi}_2\text{Te}_3$  samples arises from the change in charge carrier from p-type, in the first system, to n-type in the 2D-FM/TI [18]. Figure 2(c) shows the amplitude of the THE as a function of the applied field and temperature for the  $\text{Cr}_{1+\delta}\text{Te}_2$  (7 TL)/ $\text{Bi}_2\text{Te}_3$  sample. The white regions in the resulting phase diagram may be attributed to either the absence of chiral texture or to a low THE/AHE ratio far from the temperature of AHE sign inversion. It is also worth noting that this diagram is very reminiscent of the magnetic phase diagrams of B20 materials where it is possible to find pockets of stability of skyrmion lattices [37]. They are, however, located near the Curie temperature, unlike in the  $\text{Cr}_{1+\delta}\text{Te}_2$  case. The temperature profile of the AHE amplitude as a function of the temperature is shown in Fig. 2 (d). Simultaneously to the preparation of this manuscript, direct imaging of a skyrmion lattice in  $\text{Cr}_{1+\delta}\text{Te}_2$  has been reported through Lorentz microscopy at 100K for  $\delta=0.3$  [38].

The fact the THE-like signal peaks at the temperature at which the AHE changes sign (50 K for Al, 100 K for  $\text{Bi}_2\text{Te}_3$  capping) suggests that another explanation is possible. If one assumes a potential gradient due to interfaces, the temperature dependence of the AHE might vary, and the AHE sign reversal can occur at slightly different temperature for an interfacial portion of the  $\text{Cr}_{1+\delta}\text{Te}_2$ . A model considering a bulk and interfacial  $\text{Cr}_{1+\delta}\text{Te}_2$  “layers” with slightly different AHE temperature dependence allows all the observed signals ( $R_{xy}(H)$ ,  $R_{AHE}(T)$  and the phase diagram) to be well reproduced (see Supplementary Materials, section 5 [19]). The success of such a crude model indicates that such effect cannot be ignored and signals attributed to THE must be very carefully considered. A possible interfacial component of the AHE would be heavily dependent on the interface composition because of doping or even spin-charge interconversion phenomena. These effects could lead then to an effective shift in the temperature dependence of the interfacial component of the AHE. It may explain the temperature dependence of the AHE inversion as a function of interface composition, as observed in in Fig. 2 (d).

Although the simulation shows that a THE-like signal can be produced without topological effects arising from a chiral magnetization texture, the exact nature of the spin texture and the electronic band-structure in general at the TI/2D-FM interface is unknown. We show, however, in the next sections, that these interfacial effects are relevant for both magnetoresistance and spin-current generation phenomena in  $\text{Cr}_{1+\delta}\text{Te}_2/\text{Bi}_2\text{Te}_3$  stacks. The relative importance of interfacial effects to the electrical

transport phenomena at  $\text{Cr}_{1+\delta}\text{Te}_2/\text{Bi}_2\text{Te}_3$  bilayers points towards the possible preservation of polarized surface states at the TI/2D-FM interface.

### C. Angular dependent magnetoresistance

Figure 3 shows longitudinal magnetoresistance  $R_{xx}$  curves for  $\text{Cr}_{1+\delta}\text{Te}_2/\text{W}$  and  $\text{Cr}_{1+\delta}\text{Te}_2/\text{Bi}_2\text{Te}_3$  bilayers for different orientations of the external magnetic field at 15 K. For all samples, the magnetoresistance curves exhibit a linear decrease for in-plane fields above saturation (Figs. 3(b)-(d)), as is the case for the perpendicular orientation on the film capped by W. For  $\text{Cr}_{1+\delta}\text{Te}_2/\text{Bi}_2\text{Te}_3$  samples, however, the magnetoresistance curve exhibits a quadratic field dependence at high perpendicular field, which is a characteristic signature of the magnetoresistance response of the topological insulator film. The Lorentz magnetoresistance is visible only for fields perpendicular to the planes, strongly suggesting that the conduction mostly occurs in the plane. Magnetoresistance curves for  $\text{Bi}_2\text{Te}_3$  isolated films can be found in the supplementary material [19]. Apart from the linear negative magnetoresistance, Figures 3(b)-(d) also make clear which orientation leads to the highest resistance state at saturation. Disregarding the cases displaying quadratic behavior of the perpendicular high fields, which are associated with the TI layer, the higher resistance is found when the magnetization points in-plane but transverse to the current. This is clearly not compatible with the conventional anisotropic magnetoresistance (AMR) behavior nor standard spin-Hall magnetoresistance (SMR) [39], as we discuss hereafter. Angular scans of the longitudinal resistance ( $R_{xx}$ ) were carried out in order to directly probe contributions from AMR and SMR or additional magnetoresistance effects. Figures 3(e)-(g) show  $R_{xx}$  for scans in the  $xy$ ,  $xz$  and  $yz$  planes for the two different thickness of  $\text{Cr}_{1+\delta}\text{Te}_2$  in the heterostructure.

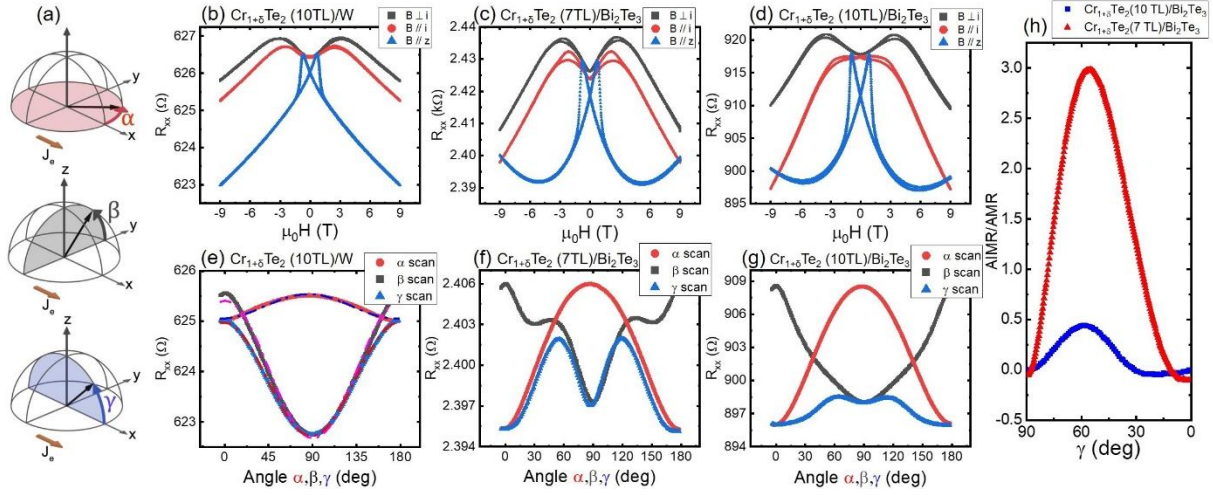


Figure 3: (a) Schematics defining the angle conventions of the magnetoresistance measurements. (b), (c), and (d) show the longitudinal resistance ( $R_{xx}$ ) as a functional of the applied field for  $\text{Cr}_{1+\delta}\text{Te}_2$  (7 ML)/W samples,  $\text{Cr}_{1+\delta}\text{Te}_2$  (7 ML)/ $\text{Bi}_2\text{Te}_3$ , and  $\text{Cr}_{1+\delta}\text{Te}_2$  (10 ML)/ $\text{Bi}_2\text{Te}_3$  respectively. (e), (f), and (g) show the longitudinal resistance for different angular sweeps following the convention of panel (a), and for a constant field of 9T. The panel (e) also shows the best cosine-squared fittings for the experimental points. In panel (h) the AIMR component as a function of the  $\gamma$  is shown for the two different  $\text{Cr}_{1+\delta}\text{Te}_2/\text{Bi}_2\text{Te}_3$  bilayers. All measurements were conducted at 15 K.

Scans in the  $xy$ ,  $xz$ , and  $yz$  planes follow the convention expressed in the schematics of Fig. 3(a). Often, the magnetoresistance can be split into different components, whose contribution is proportional to the square of the magnetization projection along orthogonal in-plane axes: either  $m_x^2$  or  $m_y^2$ , resulting in cosine-squared dependence of the angle of the magnetization relative to the current direction (see Fig. 3(a)). The most common contributions are the AMR, proportional to  $+m_x^2$ , and the SMR to  $-m_y^2$ . From the results of the  $\text{Cr}_{1+\delta}\text{Te}_2/\text{W}$  bilayer, shown in panel (e) of Fig. 3, we can observe that resistance curves can be reasonably fitted by functions proportional to the cosine squared of the respective angles. In the  $\gamma$  scan, *i. e.*, magnetic rotation in the  $x$ - $z$  plane, the maximum of resistance occurs for  $\gamma = 0^\circ/180^\circ$  ( $\mathbf{m} \parallel \mathbf{x}$ ). This behavior is compatible with a conventional *positive* contribution from AMR. Our  $\beta$  scan also exhibits a *positive* cosine squared contribution to the magnetoresistance, that is, the state of maximum resistance also occurs when the magnetization is in-plane, specifically when  $\mathbf{m} \parallel \mathbf{y}$ . A previous report [13] on the magnetoresistance of  $\text{Cr}_{1+\delta}\text{Te}_2$  described a large negative AMR, but their measurement did not take into account transversal magnetoresistance terms such as the SMR. Indeed, scanning in the  $x$ - $y$  plane, *i. e.*  $\alpha$  scans, mixes the two components and a larger positive contribution of the transversal component, as observed in our results, leads to higher resistance state when  $\mathbf{m} \parallel \mathbf{y}$ , which can be confused as a negative AMR when considering  $\alpha$  scans alone. The same large positive transversal

magnetoresistance ( $\beta$  scan) is also observed for samples of  $\text{Cr}_{1+\delta}\text{Te}_2/\text{Bi}_2\text{Te}_3$  bilayers, shown in panels (f) and (g) of Fig. 3. This positive transversal component is not compatible with traditional SMR, which are generally proportional to  $-m_y^2$ . A similar behavior has been recently observed in Ta/NiFe and Pt/NiFe bilayers and was associated to a purely interfacial contribution to the spin-to-charge interconversion phenomena [23].

The AMR contribution ( $\gamma$  scan) appears to be negative due the crossover of the  $R(H_x)$  and  $R(H_z)$  at high-fields caused by the quadratic component of the magnetoresistance of the  $\text{Bi}_2\text{Te}_3$ , as can be observed in Fig. 3 (c) and (d) around 8.5 T. However, on top of the cosine squared behavior on  $\beta$  and  $\gamma$  scans peak-like features can be observed at about  $60^\circ$  and  $120^\circ$ . These features may arise from the Anisotropic Interfacial Magnetoresistance (AIMR) [40], which is described by higher order of even-powered cosine terms. This effect is mainly associated to the scattering at ferromagnet/paramagnet interfaces and may point to the occurrence of a magnetic phase at the 2D-FM/TI interface. The interfacial characteristic of the observed peak-like features is clear when we consider ratio AIMR/AMR for samples with different thickness, as shown in Fig. 3(h). The sample with thinner FM layer displays a much larger effect, as expected from a pure interfacial effect.

#### D. Spin-orbit torques

The charge to spin conversion in the  $\text{Cr}_{1+\delta}\text{Te}_2/\text{Bi}_2\text{Te}_3$  heterostructures was probed by current-induced SOT measurements. Torque magnitudes were obtained using the second-harmonic technique [41–43]. Figure 4(a) shows a schematic view of the second-harmonic experiment and the SOT effective fields. For more details, the complete protocols for measurements can be found in the supplementary material, as well as the experimental curves and modelling for all the results discussed subsequently [19].

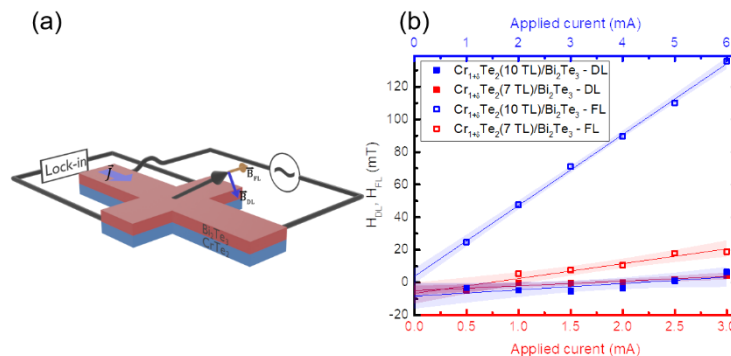


Figure 4: (a) Schematic view of the experimental setup and the torque effective field geometry. (b) Extracted DL and FL field amplitudes extracted from 2nd harmonic torque measurements at 15K as a function of the applied current. The shaded areas around the linear fittings represent the 95% confidence intervals.

Figure 4(b) shows the amplitude of FL and DL torque effective fields vs. the applied current for different bilayers, thus unambiguously demonstrating the SOT mechanism. The extracted current induced DL and FL torque effective fields were,  $H_{DL} = 12.5$  mT and  $H_{FL} = 38$  mT at an average current density of  $10^7$  A/cm<sup>2</sup> for the sample with 7 TL of Cr<sub>1+δ</sub>Te<sub>2</sub>, and  $H_{DL} = 10$  mT and  $H_{FL} = 115$  mT at  $10^7$  A/cm<sup>2</sup> for the sample with 10 TL of Cr<sub>1+δ</sub>Te<sub>2</sub>. While the magnitude of the damping-like field remains basically constant, in the order of a dozen of mT at  $10^7$  A/cm<sup>2</sup>, the FL to DL torque ratio increases to be almost 4 times larger with the increase in the FM layer thickness. The obtained DL torques values are marginally above the torque magnitudes found in transition-metal systems, such as Co/Pt, Co/Ta or Co/β-W, which are also in the order of a few mT [42,44]. However, the measured FL torque component is significantly larger, well beyond the corresponding values observed in the conventional SOT systems. Its large value evidences the predominance of the Rashba-Edelstein mechanism to charge-to-spin conversion in line with theoretical predictions [20]. This result supports the interfacial origin of the spin current generation from polarized surface states reported for the topological insulator Bi<sub>2</sub>Te<sub>3</sub> [10,45] even after the deposition of the Quasi-2D ferromagnetic material.

#### E. Magnetization reversal induced by SOT

Current induced switching experiments have also been carried out successfully in the Cr<sub>1+δ</sub>Te<sub>2</sub>/Bi<sub>2</sub>Te<sub>3</sub> bilayers. The reversal experiments were monitored via AHE measurements between pulses of current applied to samples patterned by optical lithography. The curves shown in Fig. 5(a) showing a clear current-induced magnetization reversal were obtained in the Cr<sub>1+δ</sub>Te<sub>2</sub> (10 TL)/Bi<sub>2</sub>Te<sub>3</sub> sample using pulses of 100 μs in 5-μm-wide Hall bars. Nevertheless, similar to current induced switching experiments reported for Quasi-2D Fe<sub>3</sub>GeTe<sub>2</sub>/Pt [46,47] and Cr<sub>2</sub>Ge<sub>2</sub>Te<sub>6</sub>/Pt [48], we were unable to achieve complete reversal. Only a part of the resistance curve describes a hysteretic loop as a function of current with the SOT symmetries. Even though the change in resistance is about 40 mΩ, which is comparable to the change in resistance found in all-metallic stacks, this value represents only 8% of the change in resistance between remanent states. The switching seems to be limited by

thermally induced magnetic domain nucleation since intermediary magnetic states can be reached regardless of the polarity of the current, and even in absence of an in-plane field, as shown in the inset of Fig. 5(a). Once these intermediary states are achieved, partial SOT-induced switching can be achieved as evidenced by the hysteric behavior of the AHE resistance seen in Fig. 5(b). The supplementary material also contains an optical microscopy image of the devices used in this work as well as theoretical details of the second harmonic technique for SOT evaluation [17,19,24,39,41,43,49–53].

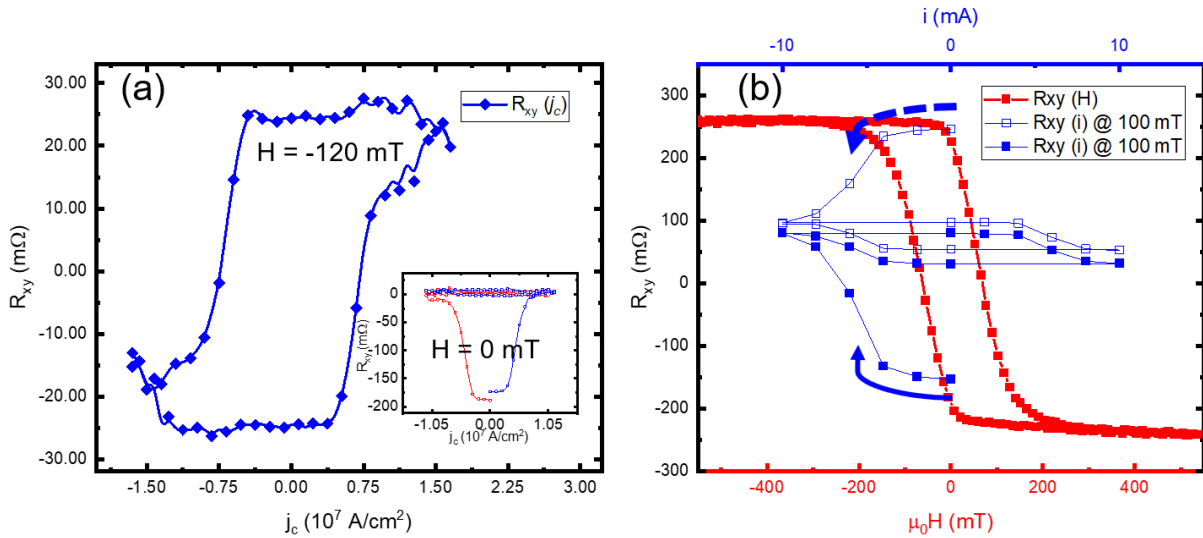


Figure 5: (a) Hall voltage a function of the pulsed current intensity at 140 K. (b) Complete switching curve departing from two different initial conditions for the experiments, namely the remanent states after either positive or negative saturation. The AHE curve at the same temperature is also shown for comparisons. For panel (a) the applied in-plane field was -120 mT while there was no field for the curves in the inset. The Hall bars were patterned from the complete sapphire/1 ML  $\text{WS}_2/\text{Cr}_{1+\delta}\text{Te}_2$  (10 TL)/ $\text{Bi}_2\text{Te}_3$  (10 QL) stack.

### 3. CONCLUSIONS

In this work, by adopting low temperature MBE growth of  $\text{CrTe}_2/\text{Bi}_2\text{Te}_3$  heterostructures, we achieved a  $\text{Cr}_{1+\delta}\text{Te}_2$  epitaxial phase on sapphire substrates/ $\text{WS}_2$  with well-defined ferromagnetic properties and PMA. Evaluation of the magnetic properties and the charge to spin conversion efficiency shows the important role of interface states. First, magneto-transport reveals the presence of an interfacial AIMR and an unexpected large positive transversal magnetoresistance attributed to spin-to-charge interconversion phenomena induced by interface electronic states. Second, the heterostructures show an unexpectedly large FL torque in second-harmonic spin torque measurements dominating the overall SOT effect. The latter result points to either the persistence of the topological surface states from the topological insulator film, or the emergence of Rashba states in the 2D-FM/TI interface. The high

efficiency of charge to spin conversion results in current induced magnetization reversal in  $\text{Cr}_{1+\delta}\text{Te}_2/\text{Bi}_2\text{Te}_3$ , which is similar to other SOT systems making this heterostructure suitable for spintronic devices. We hope that these results will stimulate the research on large scale growth of Van der Waals heterostructure including topological insulator and 2D ferromagnets dedicated to spintronic applications.

#### 4. ACKNOWLEDGEMENTS

The authors gratefully acknowledge the funding from EU H2020 FET PROAC project SKYTOP- 824123.

#### 5. REFERENCES

- [1] E. Y. Vedmedenko, R. K. Kawakami, D. D. Sheka, P. Gambardella, A. Kirilyuk, A. Hirohata, C. Binek, O. Chubykalo-Fesenko, S. Sanvito, B. J. Kirby, et al., The 2020 Magnetism Roadmap, J. Phys. Appl. Phys. 53, 453001 (2020).
- [2] Q. Shao, P. Li, L. Liu, H. Yang, S. Fukami, A. Razavi, H. Wu, K. Wang, F. Freimuth, Y. Mokrousov, et al., Roadmap of Spin–Orbit Torques, IEEE Trans. Magn. 57, 1 (2021).
- [3] M. Z. Hasan and C. L. Kane, *Colloquium* : Topological Insulators, Rev. Mod. Phys. 82, 3045 (2010).
- [4] S. Fragkos, L. Baringthon, P. Tsipas, E. Xenogiannopoulou, P. Le Fèvre, P. Kumar, H. Okuno, N. Reyren, A. Lemaître, G. Patriarche, et al., Topological Surface States in Epitaxial  $\text{Sn}_{1-x}\text{Bi}_x\text{Te}_3$  Natural van Der Waals Superlattices, Phys. Rev. Mater. 5, 014203 (2021).
- [5] H. Wu, A. Chen, P. Zhang, H. He, J. Nance, C. Guo, J. Sasaki, T. Shirokura, P. N. Hai, B. Fang, et al., Magnetic Memory Driven by Topological Insulators, Nat. Commun. 12, 6251 (2021).
- [6] N. H. D. Khang, Y. Ueda, and P. N. Hai, A Conductive Topological Insulator with Large Spin Hall Effect for Ultralow Power Spin–Orbit Torque Switching, Nat. Mater. 17, 808 (2018).
- [7] *Room-Temperature High Spin–Orbit Torque Due to Quantum Confinement in Sputtered  $\text{Bi}_x\text{Se}_{1-x}$  Films* | Nature Materials, <https://www.nature.com/articles/s41563-018-0136-z>.
- [8] J. Han and L. Liu, Topological Insulators for Efficient Spin–Orbit Torques, APL Mater. 9, 060901 (2021).
- [9] Q. Barbedienne, J. Varignon, N. Reyren, A. Marty, C. Vergnaud, M. Jamet, C. Gomez-Carbonell, A. Lemaître, P. Le Fèvre, F. Bertran, et al., Angular-Resolved Photoemission Electron Spectroscopy and Transport Studies of the Elemental Topological Insulator  $\alpha\text{-Sn}$ , Phys. Rev. B 98, 195445 (2018).
- [10] K. Hoefer, C. Becker, S. Wirth, and L. Hao Tjeng, Protective Capping of Topological Surface States of Intrinsically Insulating  $\text{Bi}_2\text{Te}_3$ , AIP Adv. 5, 097139 (2015).
- [11] B. Chen, J. Yang, H. Wang, M. Imai, H. Ohta, C. Michioka, K. Yoshimura, and M. Fang, Magnetic Properties of Layered Itinerant Electron Ferromagnet  $\text{Fe}_3\text{GeTe}_2$ , J. Phys. Soc. Jpn. 82, 124711 (2013).

- [12] D. C. Freitas, R. Weht, A. Sulpice, G. Remenyi, P. Strobel, F. Gay, J. Marcus, and M. Núñez-Regueiro, Ferromagnetism in Layered Metastable 1T-CrTe<sub>2</sub>, *J. Phys. Condens. Matter* 27, 176002 (2015).
- [13] X. Sun, W. Li, X. Wang, Q. Sui, T. Zhang, Z. Wang, L. Liu, D. Li, S. Feng, S. Zhong, et al., Room Temperature Ferromagnetism in Ultra-Thin van Der Waals Crystals of 1T-CrTe<sub>2</sub>, *Nano Res.* 13, 3358 (2020).
- [14] R. de M. T. Araujo, J. Zarpellon, and D. H. Mosca, Unveiling Ferromagnetism and Antiferromagnetism in Two Dimensions at Room Temperature, *J. Phys. Appl. Phys.* 55, 283003 (2022).
- [15] Y. Wu, S. Zhang, J. Zhang, W. Wang, Y. L. Zhu, J. Hu, G. Yin, K. Wong, C. Fang, C. Wan, et al., Néel-Type Skyrmion in WTe<sub>2</sub>/Fe<sub>3</sub>GeTe<sub>2</sub> van Der Waals Heterostructure, *Nat. Commun.* 11, 3860 (2020).
- [16] Y. Wu, B. Francisco, Z. Chen, W. Wang, Y. Zhang, C. Wan, X. Han, H. Chi, Y. Hou, A. Lodesani, et al., A Van Der Waals Interface Hosting Two Groups of Magnetic Skyrmions, *Adv. Mater.* 34, 2110583 (2022).
- [17] X. Zhang, S. C. Ambhire, Q. Lu, W. Niu, J. Cook, J. S. Jiang, D. Hong, L. Alahmed, L. He, R. Zhang, et al., Giant Topological Hall Effect in van Der Waals Heterostructures of CrTe<sub>2</sub>/Bi<sub>2</sub>Te<sub>3</sub>, *ACS Nano* 15, 15710 (2021).
- [18] J. Chen, L. Wang, M. Zhang, L. Zhou, R. Zhang, L. Jin, X. Wang, H. Qin, Y. Qiu, J. Mei, et al., Evidence for Magnetic Skyrmions at the Interface of Ferromagnet/Topological-Insulator Heterostructures, *Nano Lett.* 19, 6144 (2019).
- [19] See Supplemental Material at [URL Will Be Inserted by Publisher] for a List of Samples, a Brief Discussion on the High Temperature Growth of Samples, the Magnetic Properties of Cr<sub>1+δ</sub>Te<sub>2</sub> Films, Atomistic Simulations of Skyrmions, the THE Modelling, Results of Transport Measurements, and Results of Second Harmonic SOT.
- [20] P. M. Haney, H.-W. Lee, K.-J. Lee, A. Manchon, and M. D. Stiles, Current Induced Torques and Interfacial Spin-Orbit Coupling: Semiclassical Modeling, *Phys. Rev. B* 87, 174411 (2013).
- [21] N. Figueiredo-Prestes, S. Krishnia, S. Collin, Y. Roussigné, M. Belmeguenai, S. M. Chérif, J. Zarpellon, D. H. Mosca, H. Jaffrès, L. Vila, et al., Magnetization Switching and Deterministic Nucleation in Co/Ni Multilayered Disks Induced by Spin-Orbit Torques, *Appl. Phys. Lett.* 119, 032410 (2021).
- [22] S. Krishnia, Y. Sassi, F. Ajejas, N. Reyren, S. Collin, A. Fert, J.-M. George, V. Cros, and H. Jaffres, Large Interfacial Rashba Interaction and Giant Spin-Orbit Torques in Atomically Thin Metallic Heterostructures, arXiv:2205.08486.
- [23] M.-G. Kang, G. Go, K.-W. Kim, J.-G. Choi, B.-G. Park, and K.-J. Lee, Negative Spin Hall Magnetoresistance of Normal Metal/Ferromagnet Bilayers, *Nat. Commun.* 11, 3619 (2020).
- [24] K. Lasek, P. M. Coelho, K. Zborecki, Y. Xin, S. K. Kolekar, J. Li, and M. Batzill, Molecular Beam Epitaxy of Transition Metal (Ti-, V-, and Cr-) Tellurides: From Monolayer Ditellurides to Multilayer Self-Intercalation Compounds, *ACS Nano* 14, 8473 (2020).
- [25] X. Zhang, Q. Lu, W. Liu, W. Niu, J. Sun, J. Cook, M. Vaninger, P. F. Miceli, D. J. Singh, S.-W. Lian, et al., Room-Temperature Intrinsic Ferromagnetism in Epitaxial CrTe<sub>2</sub> Ultrathin Films, *Nat. Commun.* 12, 2492 (2021).
- [26] A. Purbawati, J. Coraux, J. Vogel, A. Hadj-Azzem, N. Wu, N. Bendiab, D. Jegouso, J. Renard, L. Marty, V. Bouchiat, et al., In-Plane Magnetic Domains and Néel-like Domain Walls in Thin Flakes of the Room Temperature CrTe<sub>2</sub> Van Der Waals Ferromagnet, *ACS Appl. Mater. Interfaces* 12, 30702 (2020).
- [27] A. L. Coughlin, D. Xie, Y. Yao, X. Zhan, Q. Chen, H. Hewa-Walpitage, X. Zhang, H. Guo, H. Zhou, J. Lou, et al., Near Degeneracy of Magnetic Phases in Two-Dimensional Chromium Telluride with Enhanced Perpendicular Magnetic Anisotropy, *ACS Nano* 14, 15256 (2020).
- [28] A. Roy, S. Guchhait, R. Dey, T. Pramanik, C.-C. Hsieh, A. Rai, and S. K. Banerjee, Perpendicular Magnetic Anisotropy and Spin Glass-like Behavior in Molecular Beam Epitaxy Grown Chromium Telluride Thin Films, *ACS Nano* 9, 3772 (2015).

- [29] A. Otero Fumega, J. Phillips, and V. Pardo, Controlled Two-Dimensional Ferromagnetism in 1T–CrTe<sub>2</sub>: The Role of Charge Density Wave and Strain, *J. Phys. Chem. C* 124, 21047 (2020).
- [30] I. H. Lee, B. K. Choi, H. J. Kim, M. J. Kim, H. Y. Jeong, J. H. Lee, S.-Y. Park, Y. Jo, C. Lee, J. W. Choi, et al., Modulating Curie Temperature and Magnetic Anisotropy in Nanoscale-Layered Cr<sub>2</sub>Te<sub>3</sub> Films: Implications for Room-Temperature Spintronics, *ACS Appl. Nano Mater.* 4, 4810 (2021).
- [31] L. Meng, Z. Zhou, M. Xu, S. Yang, K. Si, L. Liu, X. Wang, H. Jiang, B. Li, P. Qin, et al., Anomalous Thickness Dependence of Curie Temperature in Air-Stable Two-Dimensional Ferromagnetic 1T–CrTe<sub>2</sub> Grown by Chemical Vapor Deposition, *Nat. Commun.* 12, 1 (2021).
- [32] K. S. Denisov, I. V. Rozhansky, N. S. Averkiev, and E. Lähderanta, A Nontrivial Crossover in Topological Hall Effect Regimes, *Sci. Rep.* 7, 17204 (2017).
- [33] P. Li, J. Ding, S. S.-L. Zhang, J. Kally, T. Pillsbury, O. G. Heinonen, G. Rimal, C. Bi, A. DeMann, S. B. Field, et al., Topological Hall Effect in a Topological Insulator Interfaced with a Magnetic Insulator, *Nano Lett.* 21, 84 (2021).
- [34] M. Raju, A. Yagil, A. Soumyanarayanan, A. K. C. Tan, A. Almoalem, F. Ma, O. M. Auslaender, and C. Panagopoulos, The Evolution of Skyrmions in Ir/Fe/Co/Pt Multilayers and Their Topological Hall Signature, *Nat. Commun.* 10, 696 (2019).
- [35] L. Wang, Q. Feng, H. G. Lee, E. K. Ko, Q. Lu, and T. W. Noh, Controllable Thickness Inhomogeneity and Berry Curvature Engineering of Anomalous Hall Effect in SrRuO<sub>3</sub> Ultrathin Films, *Nano Lett.* 20, 2468 (2020).
- [36] D. J. Groenendijk, C. Autieri, T. C. van Thiel, W. Brzezicki, J. R. Hortensius, D. Afanasiev, N. Gauquelin, P. Barone, K. H. W. van den Bos, S. van Aert, et al., Berry Phase Engineering at Oxide Interfaces, *Phys. Rev. Res.* 2, 023404 (2020).
- [37] C. Pfleiderer, T. Adams, A. Bauer, W. Biberacher, B. Binz, F. Birkelbach, P. Böni, C. Franz, R. Georgii, M. Janoschek, et al., Skyrmion Lattices in Metallic and Semiconducting B20 Transition Metal Compounds, *J. Phys. Condens. Matter* 22, 164207 (2010).
- [38] R. Saha, H. L. Meyerheim, B. Göbel, B. K. Hazra, H. Deniz, K. Mohseni, V. Antonov, A. Ernst, D. Knyazev, A. Bedoya-Pinto, et al., Observation of Néel-Type Skyrmions in Acentric Self-Intercalated Cr<sub>1+δ</sub>Te<sub>2</sub>, *Nat. Commun.* 13, 1 (2022).
- [39] B. Han, B. Wang, Z. Yan, T. Wang, D. Yang, X. Fan, Y. Wang, and J. Cao, Determination of the Spin-Orbit Torques in Ferromagnetic–Heavy-Metal Bilayers Using Harmonic Longitudinal Voltage Measurements, *Phys. Rev. Appl.* 13, 014065 (2020).
- [40] A. Philippi-Kobs, A. Farhadi, L. Matheis, D. Lott, A. Chuvilin, and H. P. Oepen, Impact of Symmetry on Anisotropic Magnetoresistance in Textured Ferromagnetic Thin Films, *Phys. Rev. Lett.* 123, 137201 (2019).
- [41] S. Krishnia, E. Haltz, L. Berges, L. Aballe, M. Foerster, L. Bocher, R. Weil, A. Thiaville, J. Sampaio, and A. Mougin, Spin-Orbit Coupling in Single-Layer Ferrimagnets: Direct Observation of Spin-Orbit Torques and Chiral Spin Textures, *Phys. Rev. Appl.* 16, 024040 (2021).
- [42] C. O. Avci, K. Garello, M. Gabureac, A. Ghosh, A. Fuhrer, S. F. Alvarado, and P. Gambardella, Interplay of Spin-Orbit Torque and Thermoelectric Effects in Ferromagnet/Normal-Metal Bilayers, *Phys. Rev. B* 90, 224427 (2014).
- [43] S. J. Yun, E.-S. Park, K.-J. Lee, and S. H. Lim, Accurate Analysis of Harmonic Hall Voltage Measurement for Spin–Orbit Torques, *NPG Asia Mater.* 9, e449 (2017).
- [44] I. M. Miron, K. Garello, G. Gaudin, P.-J. Zermatten, M. V. Costache, S. Auffret, S. Bandiera, B. Rodmacq, A. Schuhl, and P. Gambardella, Perpendicular Switching of a Single Ferromagnetic Layer Induced by In-Plane Current Injection, *Nature* 476, 189 (2011).
- [45] C. I. Fornari, P. H. O. Rappl, S. L. Morelhão, T. R. F. Peixoto, H. Bentmann, F. Reinert, and E. Abramof, Preservation of Pristine Bi<sub>2</sub>Te<sub>3</sub> Thin Film Topological Insulator Surface after Ex Situ Mechanical Removal of Te Capping Layer, *APL Mater.* 4, 106107 (2016).
- [46] M. Alghamdi, M. Lohmann, J. Li, P. R. Jothi, Q. Shao, M. Aldosary, T. Su, B. P. T. Fokwa, and J. Shi, Highly Efficient Spin–Orbit Torque and Switching of Layered Ferromagnet Fe<sub>3</sub>GeTe<sub>2</sub>, *Nano Lett.* 19, 4400 (2019).

- [47] X. Wang, J. Tang, X. Xia, C. He, J. Zhang, Y. Liu, C. Wan, C. Fang, C. Guo, W. Yang, et al., Current-Driven Magnetization Switching in a van Der Waals Ferromagnet  $\text{Fe}_3\text{GeTe}_2$ , *Sci. Adv.* 5, eaaw8904 (2019).
- [48] M. Mogi, K. Yasuda, R. Fujimura, R. Yoshimi, N. Ogawa, A. Tsukazaki, M. Kawamura, K. S. Takahashi, M. Kawasaki, and Y. Tokura, Current-Induced Switching of Proximity-Induced Ferromagnetic Surface States in a Topological Insulator, *Nat. Commun.* 12, 1404 (2021).
- [49] G. P. Müller, M. Hoffmann, C. Dißelkamp, D. Schürhoff, S. Mavros, M. Sallermann, N. S. Kiselev, H. Jónsson, and S. Blügel, Spirit: Multifunctional Framework for Atomistic Spin Simulations, *Phys. Rev. B* 99, 224414 (2019).
- [50] S. Li, S.-S. Wang, B. Tai, W. Wu, B. Xiang, X.-L. Sheng, and S. A. Yang, Tunable Anomalous Hall Transport in Bulk and Two-Dimensional  $\text{CrTe}_2$ : A First-Principles Study, *Phys. Rev. B* 103, 045114 (2021).
- [51] L. Landau and E. Lifshitz, 3 - *On the Theory of the Dispersion of Magnetic Permeability in Ferromagnetic Bodies* Reprinted from *Physikalische Zeitschrift Der Sowjetunion* 8, Part 2, 153, 1935., in *Perspectives in Theoretical Physics*, edited by L. P. Pitaevski (Pergamon, Amsterdam, 1992), pp. 51–65.
- [52] T. L. Gilbert, A Phenomenological Theory of Damping in Ferromagnetic Materials, *IEEE Trans. Magn.* 40, 3443 (2004).
- [53] M. Hayashi, Analytical Expression for the Harmonic Hall Voltages in Evaluating Spin Orbit Torques, arXiv:1307.5603.